Computational Biomedicine

Science Exploration

Open Access Research Article

Prediction of circRNA-miRNA interaction sites based on fully convolutional neural network and gated recurrent unit

Ya Qiu, Yulu Li, Yike Zhao, Pengyu Zhou, Zhen Shen*

School of Computer and Software, Nanyang Institute of Technology, Nanyang 473004, Henan, China.

***Correspondence to:** Zhen Shen, School of Computer and Software, Nanyang Institute of Technology, Nanyang 473004, Henan, China. E-mail: zzuliszhen@163.com

Received: June 18, 2026 **Accepted:** September 20, 2026 **Published:** September 20, 2026

Cite this article: Qiu Y, Li Y, Zhao Y, Zhou P, Shen Z. Prediction of circRNA-miRNA interaction sites based on fully convolutional neural network and gated recurrent unit. Comput Biomed. 2026;1:202620. https://doi.org/10.70401/cbm.2026.0025

Abstract

Aims: Circular RNAs (circRNAs) act as vital microRNA (miRNA) sponges and participate in the pathogenesis of various complex diseases. Most existing computational methods focus on sequence-level prediction of circRNA-miRNA interactions, while few tools can accurately locate interaction sites at the nucleotide level.

Methods: In this study, we propose CMIFCG, a novel model combining fully convolutional neural networks (FCNs) and bidirectional gated recurrent units (BiGRU) for nucleotide-level prediction of circRNA-miRNA interaction sites. We adopted one-hot encoding for sequence preprocessing, utilized stacked convolutional modules to extract high-order features, and integrated BiGRU to capture sequential association features. The decoding module with skip connections restores feature maps to the original sequence size for precise site prediction. We constructed four datasets with different sequence lengths and negative samples to evaluate model performance.

Results: Experimental results show that CMIFCG achieves better performance than other baseline models, and excessive module stacking causes performance degradation. Motif analysis confirms that the predicted motifs match well with known miRNA sequences. Partial predicted interactions are further verified via public databases.

Conclusion: In summary, the CMIFCG model enables effective fine-grained identification of circRNA-miRNA interaction sites, providing a new tool for exploring circRNA regulatory mechanisms and disease-related molecular pathways.

Keywords: circRNA-miRNA interaction, fully convolutional neural network, gated recurrent unit, motif analysis

1. Introduction

Circular RNA (circRNA) is a single-stranded non-coding RNA with a unique circular structure[1,2]. This special structure reduces the influence of RNases and provides it with extremely high stability[3,4]. circRNAs participate in gene expression regulation primarily through four pathways: protein-protein translation and interaction, microRNA (miRNA) interaction, DNA interaction, and messenger RNA (mRNA) interaction[5]. Studies have shown that circRNA-miRNA interaction plays a crucial role in complex biological processes such as cell differentiation, cancer, and neurological diseases[2,6]. In non-small cell lung cancer (NSCLC), cancer progression is promoted by the regulation action between hsa_circ_0072088 and miR-1270/DNA topoisomerase II alpha (TOP2A) axis[7]. The interaction between circRNA derived from amyloid precursor protein (circAPP) and miR-1906/chloride intracellular channel 1 (CLIC1) axis can regulate microglial polarization, therefore being involved in Alzheimer's disease pathogenesis[8]. The proliferation, differentiation, and glycolysis of antler chondrocytes are regulated by the interaction between NOP2/Sun RNA methyltransferase family member 2 (NSUN2)/Aly/REF export factor (ALYREF)-mediated m5C-modified circRNA505, miRNA-127/p53 axis and lactate dehydrogenase A (LDHA)[9]. In summary, identifying circRNA and miRNA interaction sites is crucial for studying complex biological processes and discovering treatments for complex diseases.

Existing identification methods can be categorized into biological experimental methods and computational biology methods. Biological experimental methods provide reliable experimental data but require significant time, funding, and equipment, placing high demands on researchers' expertise, like chromatin immunoprecipitation (CHIP)[10], RT-quantitative real-time PCR (qPCR)[11]. On the other hand, some graph-based computational models have been proposed to predict RNA-RNA interactions[12,13]. Cao *et al.* proposed a novel method DGCLCMI to predict circRNA-miRNA interaction by using a deep graph collaboration learning model[14]. Li *et al.* proposed a graph-based model DeepCMI to predict circRNA-miRNA interaction by integrating multi-source information[15].

© The Author(s) 2026. This is an Open Access article licensed under a Creative Commons Attribution 4.0 International License (https://creativecommons.org/licenses/by/4.0/), which permits unrestricted use, sharing, adaptation, distribution and reproduction in any medium or format, for any purpose, even commercially, as long as you give appropriate credit to the original author(s) and the source, provide a link to the Creative Commons license, and indicate if changes were made.

Wei *et al.* proposed the model EGATCMI to predict circRNA-miRNA interaction by integrating transformer and Graph attention network[12]. GraCMI is a multi-hop graph structural model for circRNA-miRNA interaction prediction[16]. Furthermore, some deep learning computational models can be used for sequence-level circRNA-miRNA interaction identification. Liu *et al.* proposed a lightweight attention-based model SSCRB to identify circRNA-RNA binding protein (RBP) interaction sites by integrating Sequence and Structural Feature[17]. Cao *et al.* used a sequence structural attention model CRBPSA to predict circRNA-RBP interaction sites[18]. Although these models can perform interaction prediction and recognition, they still have shortcomings in terms of task level, recognition accuracy, and practicality. In general, researchers need to continue their in-depth research in identification to improve model prediction accuracy and practical application capabilities.

In this study, referencing pixel-level image segmentation models[19,20], we aim to achieve nucleotide-level circRNA and miRNA interaction prediction based on fully convolutional neural networks (CNN) and gated recurrent units (GRU)[21,22]. First, we use one-hot encoded sequence data; then, the feature extraction is performed by two encoding modules (CNN + Maxpooling + Dropout) and a bidirectional GRU, while data reconstruction is accomplished by three decoding modules (UpSampling + batch normalization + rectified linear unit (ReLU) + convolution) with skip connections; finally, the prediction results are obtained by sigmoid. Experimental results show that accurate nucleotide-level prediction can be achieved. Furthermore, we tested the impact of sequence length, feature capture method, and the number of CNN layers on model performance.

2. Materials and Methods

2.1 Data

The original dataset of cancer-specific circRNA-miRNA interactions used in this study was retrieved from the cancer-specific circRNA database (CSCD)2 (http://gb.whu.edu.cn/CSCD2/)[23]. Preliminary analysis indicated that grouping data solely by circRNA or miRNA yielded inadequate training samples for deep learning models, thereby compromising model performance. To address this issue, we first classified all data by cell line and then merged all miRNA interaction sites mapped to the same circRNA transcript. We then extended 50 nucleotides both upstream and downstream from the midpoint of each miRNA interaction region, generating circRNA-miRNA interaction sample sequences of 101 bp in length. Negative samples were derived from two sources: (1) non-interacting regions within the aforementioned interaction sample sequences; (2) length-matched sequences extracted from regions flanking the binding sites. To further evaluate the effect of input sequence length on model performance, we also generated interaction sequences of 201 bp using the same processing pipeline. Finally, Cluster Database at High Identity with Tolerance (CD-HIT) was employed to eliminate redundant sequences in both positive and negative sample sets.

Depending on the input sequence length and negative samples source, the datasets used in this study are categorized into four types, namely Data1, Data2, Data3, and Data4, as summarized in Table 1.

Table 1. Detail about dataset used in this study.

Dataset	Detail
Data1	The sequence length is 101, and the negative sample source is Source1.
Data2	The sequence length is 101, and the negative sample source is Source2.
Data3	The sequence length is 201, and the negative sample source is Source1.
Data4	The sequence length is 201, and the negative sample source is Source2.

2.2 Model workflow

The proposed model is mainly composed of FCN and GRU, divided into encoding and decoding stages. The encoding stage contains three layers: the first two layers are each constructed as a composite module comprising a convolutional layer, Maxpooling layer, ReLU, and dropout layer; the third layer integrates GRU with dropout. The decoding stage contains four layers: from bottom to top, the first three layers each consist of UpSample, batch normalization (BN), ReLU, and convolutional layers; the final layer applies a sigmoid activation function to predict interaction site labels. Additionally, the model fuses deep semantic information and shallow structural features via a skip-connection mechanism to further enhance predictive performance. The overall model architecture is illustrated in Figure 1. The code is available at: https://github.com/szhh521/CMIFCG.

2.2.1 Data preparing

In this step, we use one-hot encoding $A(1,0,0,0)$, $C(0,1,0,0)$, $G(0,0,1,0)$, $U(0,0,0,1)$ to transform the input binding site region sequence *ISeq* into a matrix that can be processed by a deep learning model. Assuming the input sequence length is L, after one-hot encoding, the input sequence is transformed into an $L*4$ matrix *ISeqM*.

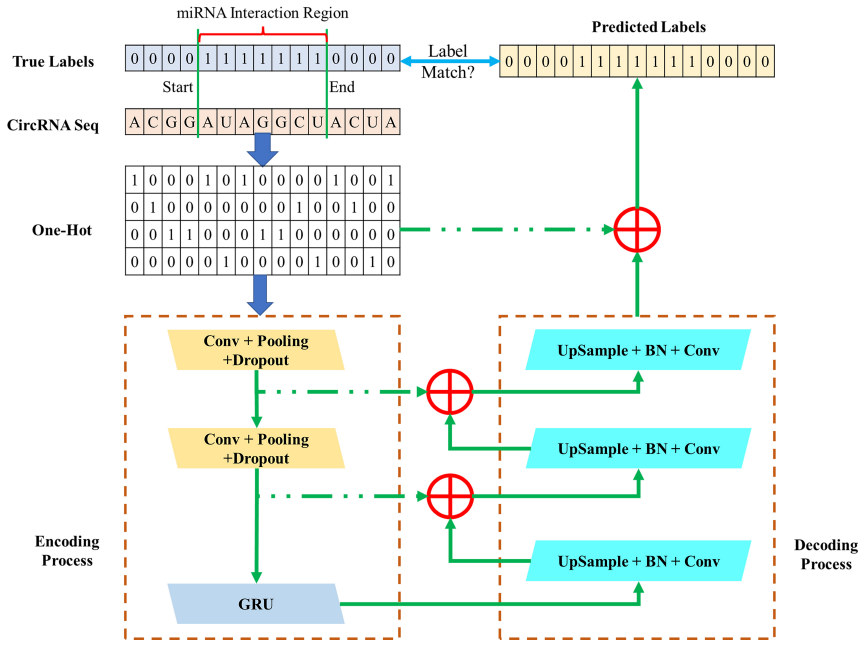


Figure 1. Model Architecture. circRNA: circular RNA; miRNA: microRNA; BN: batch normalization; GRU: gated recurrent unit; Conv: convolutional layer.

2.2.2 Feature encoding

In the feature encoding stage, successive module stacking enables higher-level convolutions to capture a broader receptive field and extract high-order features from the input data. The workflow of the feature learning module is defined as Equation 1:

$$\begin{aligned} cvout &= Conv(ipd, k, b, relu) \\ mpout &= Maxpooling(cvout) \\ dpout &= Dropout(mpout) \end{aligned} \tag{1}$$

where, *ipd* represents the input data. The first feature learning module receives *ISeqM* as its input data, while the subsequent module uses the output of the previous feature learning module as their input data. k represents the convolution kernel, and b represents the bias term during the convolution operation.

To capture correlation features among short sequences across distinct regions of the input sequence, we use the GRU to extract long-term features from the high-order features generated by the feature learning module, and adopt dropout to mitigate overfitting.

$$\begin{aligned} gruout &= BiGRU(ibg) \\ gdpout &= Dropout(gruout) \end{aligned} \tag{2}$$

where *ibg* represents the input data of the *BiGRU* layer, this layer uses the output of the previous feature learning module as its input data.

2.2.3 Feature decoding

The decoding process aims to UpSample the high-order features extracted by the encoding module to restore an output map with the same spatial dimensions as the input. Meanwhile, a skip-connection mechanism is incorporated to enhance feature representation during decoding. Each decoding module is composed of an UpSample layer, a BN layer, a ReLU activation layer, and a convolutional layer (Conv):

$$\begin{aligned} upout &= UpSample(idedata) \\ bnout &= Bat_Norm(upout) \\ reout &= Relu(bnout) \\ dcvout &= Conv(reout, k, b) \end{aligned} \tag{3}$$

where, k denotes the convolution kernel, and b denotes the bias term in the convolution operation. The UpSample layer employs linear interpolation to restore data to the designated spatial size.

Skip-connections enrich the model's feature representation during the decoding stage. Each skip-connection takes two inputs, and its computation is defined in Equation (4).

$$SKOut = EMout + DecM(Ip) \quad (4)$$

where *EMout* represents the input data from the encoding module, *DecM* represents the decoding module, *Ip* represents the decoding module input data.

In Figure 1, each circled red plus sign denotes one skip-connection operation. From bottom to top, one input of the first skip-connection is the output of the second encoding module, and the other input is the output of the GRU layer. The two inputs of the second skip-connection are the output from the preceding skip-connection and the output of the first encoding module, respectively. The two inputs of the third skip-connection correspond to the output from the preceding skip-connection and the input data. Through up-sampling and the skip-connection, the three modules work collaboratively in sequence to gradually reconstruct the dimensionality of outputs from the encoding-side GRU layer to match that of the input data for final prediction.

2.2.4 Prediction

The input data for this stage is derived by fusing the output of the top-level decoding module with the original input data matrix. The model performs base-level prediction to determine whether each position interacts with the corresponding miRNA, which can be formulated as a base-level binary classification task. Therefore, we employ the sigmoid function to generate the final prediction score: *CMIP=Sigmoid(dcvout)*.

3. Results and Discussion

3.1 Parameter settings

In this study, the key parameters of the CMISFCG model are shown in Table 2. Details of model parameters are shown in CMIFCG's github site. During model training, Adam was used to optimize the training process. Early stopping and dropout were used to prevent overfitting, with the number of early stopping epochs set to 10. The maximum number of training iterations was set to 100, and the batch size was set to 50. To fully utilize data resources and improve model robustness and stability during training, we used a five-fold cross-validation method. To evaluate model performance, in addition to the four metrics, area under the curve (AUC), F1, Precision, and Recall, we also used intersection over union (IoU). IoU is a commonly used measure in image segmentation, which represents the overlapping ratio of the predicted labels and the true labels. IoU_0 represents the ratio of predicted label 0 and true label 0. IoU_1 represents the ratio of predicted label 1 and true label 1. Mean IoU represents the average of IoU_0 and IoU_1.

Table 2. Model parameter.

Hardware information			**Software information**		
OS		Ubuntu 20.04 LTS	**Torch**		1.13.1
CPU		E5-2680V4 x2	**CUDA**		535.86.05
Memory		128G	**CUDNN**		8.9.3.28
GPU		2080Ti			
Model Parameter					
Encoding Process			**Decoding Process**		
Layer1	Conv	filters=128, ks=5	Layer1	Upsample	BILINEAR
	MP	(2,2)		Conv	filters=128, ks=3
	Dropout	0.1			
Layer2	Conv	filters=128, ks=5	Layer2	Upsample	BILINEAR
	MP	(2,2)		Conv	filters=4, ks=3
	Dropout	0.1			
GRU	BiGRU	Units=64, return_sequences=True	Layer3	Upsample	BILINEAR
	Dropout	0.1		Conv	filters=1, ks=3

BiGRU: bidirectional gated recurrent unit; GRU: gated recurrent unit; Conv: convolutional layer; OS: operating system; CPU: central processing unit; CUDA: compute unified device architecture; cuDNN: CUDA Deep Neural Network library.

3.2 Experimental results

3.2.1 Data type has a significant impact on model performance

Figure 2 presents the average, minimum, and maximum of interaction region length comparison across different cell lines. Figure 3 compares the performance of the proposed CMIFCG on Data1, Data2, Data3, and Data4. As illustrated in Figure 3, for the input length of 101, the model trained on Data1 achieves better performance in terms of F1-score, Precision, Recall, Mean IoU, and IoU_1 than that trained on Data2. This is because the interaction regions are substantially longer than non-interacting regions in Data1. By contrast, Data2 contains abundant non-interacting sites and introduces substantial interfering information, which hinders the recognition of true interaction sites. Although the model obtains an enhanced capability to distinguish non-interacting regions, IoU_0 on Data2, its detection performance, IoU_1 for interaction regions is compromised.

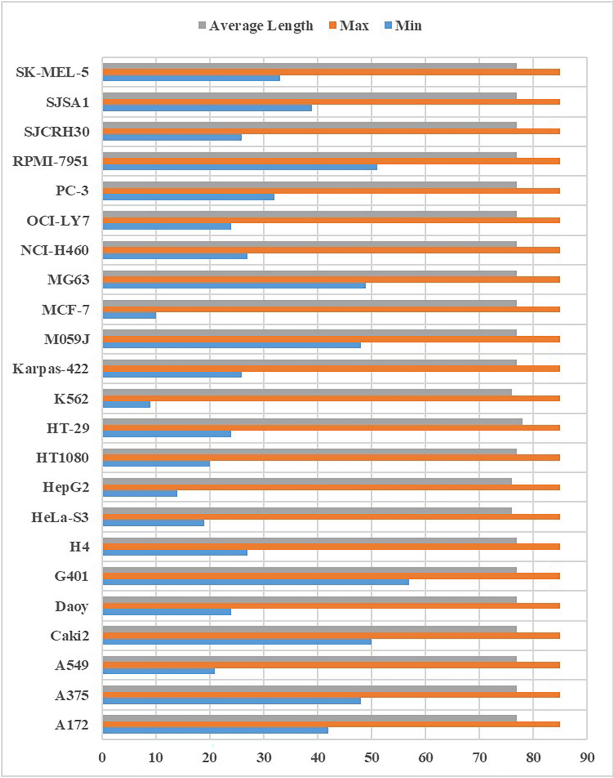


Figure 2. Interaction region length comparison across different cell lines.

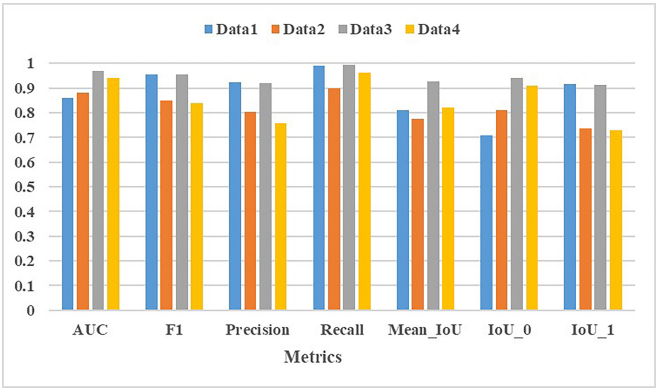


Figure 3. Model performance comparison with different input data. IoU: intersection over union; AUC: area under the curve.

When the input sequence length is extended to 201, compared with the model trained on Data1 and Data2, the model trained on Data3 yields a notable improvement in identifying both interaction and non-interacting regions. This can be attributed to the fixed intrinsic length of circRNA-miRNA interaction sites, where the extended upstream and downstream sequences supply abundant contextual feature information. For Data4, the massive inclusion of non-interacting background information results in no performance gain on interaction regions even at the input length of 201.

In conclusion, the comparison between Data2 and Data4 demonstrates that simply incorporating additional non-interacting sequences cannot effectively boost model performance. Compared with the model trained on Data1, Data3 provides sufficient original contextual information for feature learning, enabling the model to accurately recognize circRNA-miRNA interaction regions.

3.2.2 CMIFCG outperforms other baseline models

To evaluate model performance, six models, namely CRBPSA[18], GGCRB[24], MGFCRS[25], iCirc-DHN[26], CMITF and CMIAtt, were adopted as baseline models. Considering the hardware and software requirements for training all comparative models, Data1 was utilized for performance evaluation. It should be noted that CRBPSA, GGCRB, MGFCRS, and iCirc-DHN were originally designed for sequence-level prediction tasks. We modified the output layers of these four models to adapt them to base-level prediction. In addition, we adjusted the architecture of CMIFCG and tested the performance of Transformer- and attention-based structures. Table 3 summarizes the comparative performance of these models.

Table 3. Performance comparison of CMIFCG and other six baseline models.

	AUC	F1	Precision	Recall	Mean_IoU	IoU_0	IoU_1
CMIFCG	0.861+/-0.0051	0.9556+/-0.0025	0.9235+/-0.0042	0.99+/-0.0009	0.8119+/-0.0072	0.7088+/-0.0098	0.915+/-0.0046
CRBPSA	0.8586+/-0.0051	0.9556+/-0.0025	0.9219+/-0.0043	0.9919+/-0.001	0.8108+/-0.0071	0.7065+/-0.0098	0.915+/-0.0045
GGCRB	0.8414+/-0.0141	0.9252+/-0.0213	0.9255+/-0.0046	0.9272+/-0.0435	0.742+/-0.0445	0.6217+/-0.0532	0.8624+/-0.0359
MGFCRS	0.8395+/-0.0091	0.9207+/-0.0129	0.9269+/-0.0047	0.9151+/-0.0273	0.7267+/-0.0276	0.6+/-0.0333	0.8533+/-0.022
iCirc-DHN	0.8592+/-0.0068	0.9497+/-0.0088	0.9255+/-0.0048	0.9757+/-0.0196	0.7973+/-0.0217	0.6902+/-0.028	0.9045+/-0.0155
CMITF	0.8148+/-0.029	0.8938+/-0.0337	0.9205+/-0.0098	0.8745+/-0.0519	0.6863+/-0.051	0.5591+/-0.0532	0.8135+/-0.0496
CMIAtt	0.5+/-0.0	0.8674+/-0.0027	0.7659+/-0.0041	1.0+/-0.0	0.383+/-0.0021	0.0+/-0.0	0.7659+/-0.0041

AUC: area under the curve; IoU: intersection over union.

As shown in Table 3, CMIFCG achieves better overall performance than the other competing models. Compared with CMIFCG, CRBPSA, GGCRB, MGFCRS, and iCirc-DHN possess relatively complex encoders and feature-learning modules. Given identical input data, CMITF yields superior performance over CMIAtt owing to the powerful feature-learning capability of the Transformer. This indicates that complex encoders and feature-learning modules do not necessarily improve model performance. Therefore, different encoder and feature-learning modules should be tested according to task characteristics to select the combination that delivers optimal performance.

3.2.3 Adding feature analysis module has no impact on model performance

In the encoding process, the convolution kernel size is fixed. High-order feature extraction is therefore realized by stacking convolutional layers to expand the receptive field of convolutional kernels. Inspired by this principle, the encoding modules in this study are constructed in a stacked manner. The decoding module is responsible for feature reconstruction. By adopting a skip-connection mechanism, the reconstructed features from shallow decoding modules are fused with the corresponding output features of the encoding modules. This design enables deeper decoding modules to achieve more accurate feature reconstruction and consequently yield reliable prediction results. To investigate the effect of stacked module depth on model performance, we systematically compared model configurations with different numbers of stacked functional modules combined with a GRU layer, as illustrated in Figure 4.

As shown in Figure 4, simply stacking additional functional modules fails to improve model performance despite the enlarged receptive field of deeper layers; on the contrary, predictive performance gradually degrades with increasing stack depth. The two-layer structure integrated with a GRU achieves the optimal overall performance among all comparative architectures. This finding indicates that blind stacking of network modules cannot bring performance gains. Instead, comprehensive experimental validation across diverse network configurations is indispensable for determining the optimal module architecture.

3.2.4 GRU is important for feature extracting

Local association features of short subsequences within circRNA are critical for functional site identification. Although high-level convolution kernels have a wide view field, the inherent computational characteristics of CNNs limit their capability to capture such local association features. In this section, the high-level convolutional outputs are separately processed via the GRU and average pooling (AP), and the corresponding model performance is comparatively analyzed, as presented in Figure 5.

As shown in Figure 5, for both input sequence lengths of 101 and 201, the models integrated with GRU or AP achieve superior performance compared with the baseline CNN, only model. Owing to the powerful capability of GRU in capturing sequential

association features, the model using FCN and GRU exhibits a notable performance advantage.

3.2.5 Motif found by CMIFCG match the known miRNA in miRBase

To explore the regulatory mechanisms related to CircRNAs, it is essential to accurately identify circRNA-miRNA interaction sites. In this research, we initially transform the output from the first convolution layer into position probability matrices (PPMs), followed by utilizing TOMTOM for the comparison between these PPMs and known motifs. The entire process can be elaborated through the three steps outlined below:

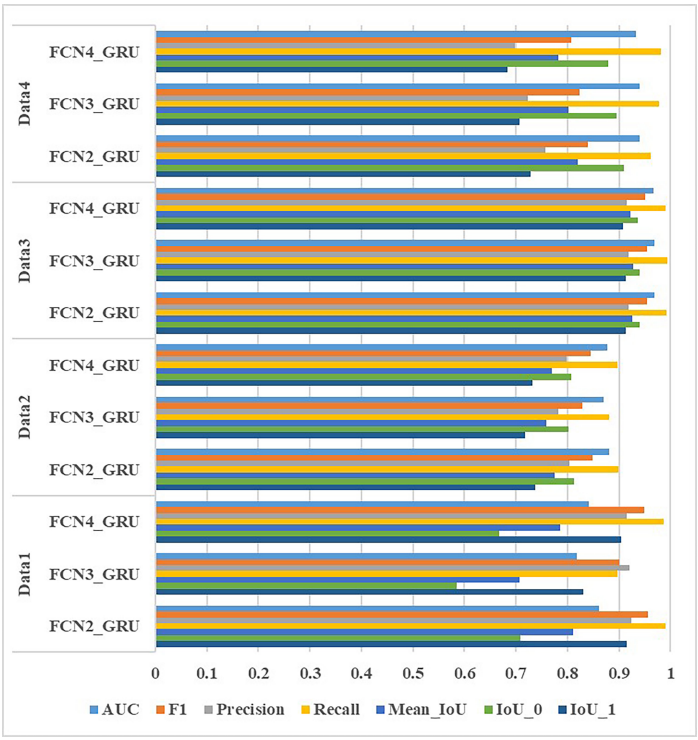


Figure 4. Model performance comparison with different stacked module depth. GRU: gated recurrent unit; FCN: fully convolutional neural network.

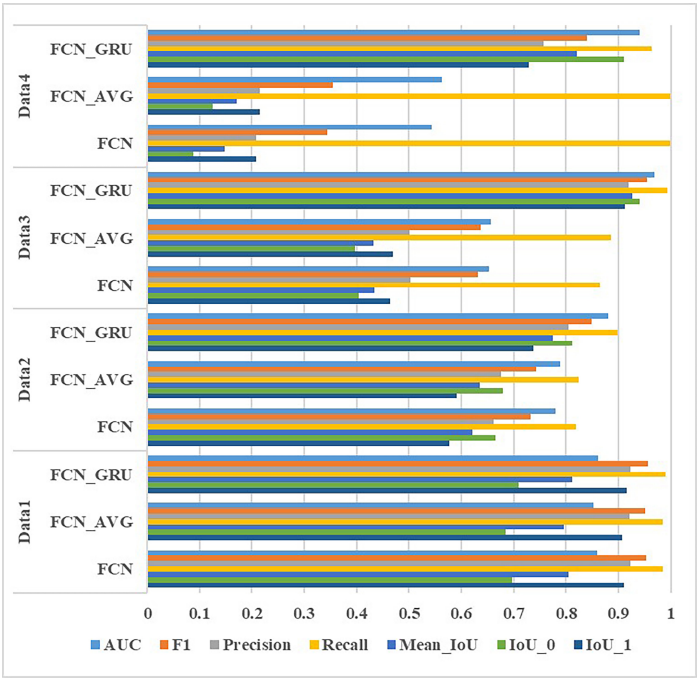


Figure 5. Model performance comparison with different feature extracting methods. GRU: gated recurrent unit; FCN: fully convolutional neural network; IoU: intersection over union; AUC: area under the curve.

1) Input data→candidate motif evaluation matrix (CMEM): The output of the first convolution layer is defined as the CMEM set. Each component in the CMEM is a probability value produced by a convolution kernel, serving to reflect whether a specific subsequence qualifies as a motif.

2) CMEM→PPM: Relying on the evaluation scores contained in the CMEM, a substantial number of subsequences are obtained from all positive samples. Each CMEM corresponds to a unique PPM. The calculation of a PPM involves first counting the number of each nucleotide at every position, and then dividing this count by the total number of subsequences to obtain the normalized value.

3) PPM→motif logo: During this step, the PPMs are submitted to TOMTOM, which is used to conduct motif comparison and generate motif logos.

For miRNA motif analysis, the known miRNA motif databases retrieved from the Multiple EM for Motif Elicitation (MEME) Suite were utilized, specifically Homo_sapiens_hsa.meme. It is important to note that the motifs discussed in this section as well as the subsequent section were identified by CMIFCG, which achieved the optimal performance in 5-fold cross-validation. A subset of the miRNA motifs detected by CMIFCG is presented in Table 4 and Figure 6, while the remaining motifs are provided in Tables S5-S27.

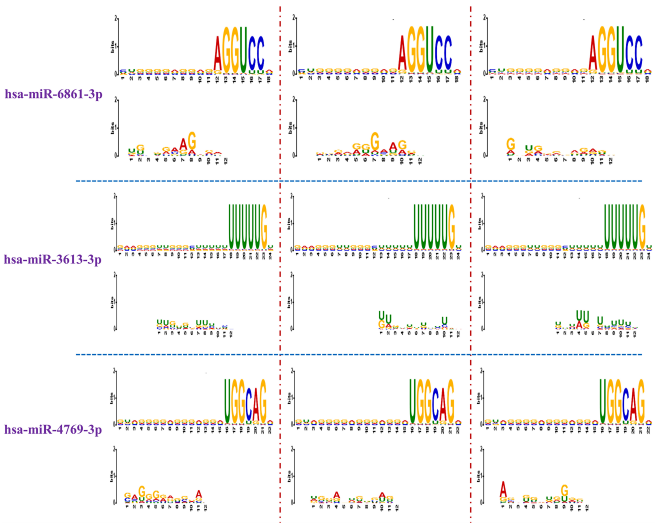


Figure 6. Sequence logos of three miRNAs matched motifs in different cell line. miRNAs: microRNAs.

Table 4. miRNA motifs found by CMIFCG match known miRNA sequence by TOMTOM.

Motif found by CMIFCG	Known miRNA in database	Known miRNA sequence	Known miRNA	Disease	E-value	Ref
UGUGCACUGUGA	MIMAT0000680	AUCUGCACUGUCAGCACUUUA	hsa-miR-106b-5p	Cervical Cancer	0.0186848	[27]
GUGGGGAAAGGG	MIMAT0005580	CUGGGGAAAAGGGUGGCACG	hsa-miR-1227-3p	osteosarcoma	0.00944169	[28]
AAGUGGGUGCAG	MIMAT0003317	GAAGGAAGUGAGUGCAGCCAC	hsa-miR-647	Glioblastoma	0.0244045	[29]
UGUGAAUCCGUU	MIMAT0000440	CAGCUGCUUUUGGGAUUCCGUUG	hsa-miR-191-5p	brain glioma	0.0126101	[30]
CCCCUCCCCACC	MIMAT0019043	CUCCCCUCACCUCCUGCUG	hsa-miR-6165	hepatocellular carcinoma	0.0616842	[32]
GUGGCUCAGGAG	MIMAT0005863	GAGGCUCAGAAUGGCUCAGGAG	hsa-miR-1200	osteosarcoma	0.00925125	[35]
GGAACUUCGACA	MIMAT0000084	GCGGAACUUAGCCACUGUGAA	hsa-miR-27a-3p	Acute myocardial infarction	0.0493487	[37]
UGCUGCUGUGUU	MIMAT0020957	GCAAAGGUAAUUGCUGUUUUCG	hsa-miR-570-3p	pediatric acute myeloid leukemia	0.142963	[38]
GAUGAGGAUUUU	MIMAT0000710	AUAAGGAUUUUUAGGGGCAUUA	hsa-miR-365a-3p	degenerative muscle disease	0.049077	[39]

miRNA: microRNA.

In living organisms, circRNAs act as molecular sponges for miRNAs. By regulating miRNA expression, circRNAs directly and indirectly modulate diverse biological processes and exert vital effects on complex diseases including cancer as well as cardiovascular and cerebrovascular diseases[27-36]. In acute myocardial infarction, EIF4A3-induced hsa_circ_0005972 exacerbates hypoxia-induced injury in H9c2 cells by targeting the miR-27a-3p/BCL2 interaction protein 3 (BNIP3) pathway, suggesting that circ-BNIP3 may serve as a novel target for alleviating hypoxia-mediated damage to cardiomyocytes[37]. Knockdown of exosomal circ_0004136 suppresses malignant progression in acute myeloid leukemia (AML) cells largely via the miR-570-3p/tetraspanin 3 (TSPAN3) axis. This finding suggests a new therapeutic approach for AML[38]. The circRNA FUT10/miR-365a-3p/HOXA9 axis regulates the regeneration of aged skeletal muscle stem cells and represents a viable therapy for degenerative muscle diseases[39]. circLRRC7 acts as a tumor suppressor in glioblastoma (GBM) and is closely linked to the expression of miR-1281 and pyridoxal phosphatase (PDXP), which provides new potential therapeutic targets for GBM therapy[40].

It should be noted that the CSCD database only provides genomic location information for circRNAs but lacks their standard nomenclature. Therefore, specific circRNA identifiers are not listed in Figure 6, Table 4, or other contents. The associations between circRNA, miRNA, and disease presented in Table 4 were verified via biological experiments. Considering factors such as untimely data updates and information inconsistency, not all prediction results can be retrieved from the databases. To further validate the model-predicted structures, we attempted to retrieve literature data relevant to all prediction results using Google Scholar and Web of Science. Table 5 shows partial references and their corresponding DOIs regarding circRNA-miRNA interactions and disease associations. All information associated with the prediction results is provided in Tables S5-S27. At the time of literature retrieval completion, all included publications were accessible and had not been retracted. Generally speaking, only a fraction of circRNA-miRNA interactions have been experimentally validated to be associated with complex diseases, while numerous unvalidated interaction data remain to be explored, which will be the focus of our future research.

Table 5. circRNA-miRNA interaction confirmed by Paper and Ref.

circRNA	miRNA	Paper Title	Ref.
circNFATC3	hsa-miR-548I	circNFATC3 sponges miR-548I acts as a ceRNA to protect NFATC3 itself and suppressed hepatocellular carcinoma progression	[41]
Hsa_circ_0062682	hsa-miR-940	Hsa_circ_0062682 promotes serine metabolism and tumor growth in colorectal cancer by regulating the miR-940/PHGDH axis	[42]
CircC6orf132	hsa-miR-873-5p	CircC6orf132 facilitates proliferation, migration, invasion, and glycolysis of gastric cancer cells under hypoxia by acting on the miR-873-5p/PRKAA1 axis	[43]
Circ_0061140	hsa-miR-126-5p	Circ_0061140 potentiates clear cell renal cell carcinoma progression via the microRNA-126-5p/ADAM9 axis	[44]
circCCDC85A	hsa-miR-550a-5p	Circular RNA circCCDC85A inhibits breast cancer progression via acting as a miR-550a-5p sponge to enhance MOB1A expression	[45]
CircRhoC	hsa-miR-302e	CircRhoC promotes tumorigenicity and progression in ovarian cancer by functioning as a miR-302e sponge to positively regulate VEGFA	[46]
CircTBC1D22A	hsa-miR-1825	CircTBC1D22A inhibits the progression of colorectal cancer through autophagy regulated via miR-1825/ATG14 axis	[47]
Hsa_circ_0123190	hsa-miR-483-3p	Hsa_circ_0123190 acts as a competitive endogenous RNA to regulate APLNR expression by sponging hsa-miR-483-3p in lupus nephritis	[48]
CircFBXL5	hsa-miR-216b	CircFBXL5 promotes the 5-FU resistance of breast cancer via modulating miR-216b/HMGA2 axis	[49]
circBRCA1	hsa-miR-642a-5p	M6A demethylase FTO-stabilized exosomal circBRCA1 alleviates oxidative stress-induced granulosa cell damage via the miR-642a-5p/FOXO1 axis	[50]
hsa_circRNA_002178	hsa-miR-328-3p	Circular RNA hsa_circRNA_002178 silencing retards breast cancer progression via microRNA-328-3p-mediated inhibition of COL1A1	[51]
circRUNX1	hsa-miR-449b-5p	IGF2BP2-induced circRUNX1 facilitates the growth and metastasis of esophageal squamous cell carcinoma through miR-449b-5p/FOXP3 axis	[52]

circ_0000020	hsa-miR-142-5p	Circular RNA circ_0000020 promotes osteogenic differentiation to reduce osteoporosis via sponging microRNA miR-142-5p to up-regulate Bone Morphogenetic Protein BMP2	[53]
CircHIPK3	hsa-miR-876-5p	CircHIPK3/miR-876-5p/PIK3R1 axis regulates regulation proliferation, migration, invasion, and glutaminolysis in gastric cancer cells	[54]
hsa_circ_0007142	hsa-miR-103a-2-5p	Circular RNA hsa_circ_0007142 is upregulated and targets miR-103a-2-5p in colorectal cancer	[55]
circESYT2	hsa-miR-665	Circular RNA circESYT2 serves as a microRNA-665 sponge to promote the progression of hepatocellular carcinoma through ENO2	[56]

circRNA-miRNA: circular RNA-microRNA.

For future biomedical research, we plan to carry out studies in two main directions. First, we will collect more datasets of circRNA-miRNA interactions from public databases and published literature to further validate the prediction performance of our model. Second, with patients' informed consent, we will collaborate with hospitals to acquire and analyze disease-related sequence data and interactive regulatory information of circRNAs and miRNAs. Comparative analyses based on the above two research strategies will not only verify the known disease-associated circRNA-miRNA regulatory interactions but also help discover novel regulatory pathways and identify potential therapeutic targets for cancer.

4. Limitations

CircRNA-miRNA interactions govern core biological processes and disease pathogenesis. Existing validation methods suffer from high cost and low throughput, while mainstream computational tools merely realize coarse sequence-level prediction without precise single-base localization. To fill this gap, we developed CMIFCG, a hybrid FCN-GRU framework dedicated to base-level detection of circRNA-miRNA binding sites. Its stacked convolution modules extract multi-scale sequence features, BiGRU captures long-distance sequential correlations, and skip connections fuse multi-layer features for accurate site reconstruction.

Systematic ablation experiments prove that CMIFCG achieves better performance than other baseline models; deeper stacked modules trigger overfitting and performance decline. Moderately lengthening input sequences provides richer contextual cues and boosts detection accuracy, whereas excessive non-interacting background sequences introduce noise and impair model sensitivity. Motif matching against public miRNA databases validates the reliability of CMIFCG's predictions, and numerous detected circRNA-miRNA pairs are strongly associated with multiple human disorders. This work is limited by incomplete cross-database annotation and inconsistency, which restricts large-scale verification of predicted interactions.

Beyond cross-database annotation discrepancies, our study has several additional noteworthy limitations. First, all training and test samples in this work are derived from cancer-related circRNA datasets retrieved from CSCD. The model is trained predominantly on cancer-derived sequence data, which may lead to potential dataset bias and could reduce generalization performance when applied to circRNAs from non-cancer tissues or diseases. Second, CMIFCG is a sequence-driven prediction model that relies exclusively on nucleic acid sequence information. It does not incorporate biological context such as tissue-specific expression profiles, RNA secondary-structure features, or epigenetic modification signals. Sequence-only input cannot fully reflect the real-world circRNA-miRNA binding environment inside living cells. Third, although we performed motif-level validation and literature-based verification for partial prediction results, large-scale wet-lab experimental validation (such as RT-qPCR or RNA-pull-down assays) for the base-level predicted binding sites is still lacking. Computational outputs require further biochemical experimental confirmation to confirm genuine physical binding events. Fourth, our model cannot distinguish functional versus non-functional binding sites. Even if a nucleotide-level binding site is predicted, it remains unknown whether this interaction exerts actual regulatory effects on downstream biological processes.

In addition to the above-mentioned limitations, purely sequence-driven prediction also lacks multi-level biological context. Therefore, introducing RNA-specialized pre-trained large-language models and multi-omics data fusion are promising strategies to compensate for the missing biological contextual information and improve the biological interpretability of prediction outputs.

5. Conclusions

In this study, we propose CMIFCG, a hybrid model combining fully convolutional neural networks and bidirectional gated recurrent units for nucleotide-level prediction of circRNA-miRNA interaction sites. Equipped with convolutional feature extraction, BiGRU, and skip connections, the model achieves fine-grained localization of interaction sites. Experimental results demonstrate that the two-layer FCN-BiGRU architecture yields optimal performance, while excessive module stacking causes performance degradation. Appropriate extension of input sequence length enriches contextual information and improves detection accuracy, yet abundant

non-interacting sequences bring interference and weaken model performance. Motif analysis verifies that the predicted motifs match well with known miRNA sequences, and many identified interaction pairs are closely linked to various human diseases.

For future research, we mainly focus on three research directions. First, we will further optimize the overall performance of CMIFCG by adjusting network architectures and hyper-parameter combinations to improve its accuracy and generalization ability for circRNA-miRNA interaction-site identification. Second, incorporating pre-trained RNA-oriented large language models represents a promising optimization route. Pre-trained RNA large-language models have learned massive implicit RNA sequence and structural patterns from extensive transcriptomic data[57,58]. Integrating such pre-trained encoders into our CMIFCG framework can supplement intrinsic RNA structural and contextual information that cannot be fully captured by pure convolutional-recurrent architectures. This may mitigate limitations caused by limited training-data volume and further boost the generalization capacity on unseen circRNA sequences. Third, multi-omics data integration is another valuable future direction. Multi-omics datasets including transcriptomics, epigenomics, and mutation profiles can provide complementary biological evidence. By combining our base-level interaction-site prediction results with multi-omics profiles, we can systematically construct circRNA-associated regulatory networks. This enables deeper investigation of circRNA-miRNA sponging mechanisms, the functional consequences of circRNA mutations on miRNA-binding affinity, and downstream gene-expression perturbations linked to disease phenotypes. Such multi-omics-driven analysis helps translate computational site-level predictions into interpretable biological hypotheses for wet-laboratory experimental validation.

Supplementary materials

The supplementary material for this article is available at: Supplementary materials.

Declarations

Authors contribution

Qiu Y, Shen Z: Conceptualization, writing-original draft, writing-review & editing.
Li Y, Zhao Y, Zhou P: Formal analysis.

Conflicts of interest

The authors declare no conflicts of interest.

Ethical approval

Not applicable.

Consent to participate

Not applicable.

Consent for publication

Not applicable.

Availability of data and materials

The source code of CMIFCG and the sample data used in this study are available at https://github.com/szhh521/CMIFCG. Additional data and materials are available from the corresponding author upon reasonable request.

Funding

This work was supported by the National Natural Science Foundation of China (Grant Nos. 62102200, 62502242, 62472239, 62372255, 62402250, and 62002189) and partly supported by Natural Science Foundation of Henan, China (Grant Nos. 262300421803 and 252300423330).

Copyright

© The Author(s) 2026.

References

1. Liu CX, Chen LL. Circular RNAs: Characterization, cellular roles, and applications. Cell. 2022;185(12):2016-2034. [DOI][PubMed]
2. Singh S, Sinha T, Panda AC. Regulation of microRNA by circular RNA. Wiley Interdiscip Rev RNA. 2023;15(1):e1820. [DOI][PubMed]
3. Niu M, Chen Y, Wang C, Zou Q, Xu L. Computational approaches for circRNA-disease association prediction: A review. Front Comput Sci.

2024;19(4):194904. [DOI]
4. Zhang J, Zhao F. Circular RNA discovery with emerging sequencing and deep learning technologies. Nat Genet. 2025;57(5):1089-1102. [DOI]
5. Nemeth K, Bayraktar R, Ferracin M, Calin GA. Non-coding RNAs in disease: From mechanisms to therapeutics. Nat Rev Genet. 2024;25(3):211-232. [DOI][PubMed]
6. Panda AC. Circular RNAs act as miRNA sponges. In: Xiao J, editor. Circular RNAs: Biogenesis and functions. Singapore: Springer; 2018. p. 67-79. [DOI]
7. Li S, Cui Z, Gao M, Shan Y, Ren Y, Zhao Y, et al. Hsa_circ_0072088 promotes non-small cell lung cancer progression through modulating miR-1270/TOP2A axis. Cancer Cell Int. 2025;25(1):156. [DOI]
8. Wu DP, Wei YS, Hou LX, Du YX, Yan QQ, Liu LL, et al. Circular RNA APP contributes to Alzheimer's disease pathogenesis by modulating microglial polarization via miR-1906/CLIC1 axis. Alzheimers Res Ther. 2025;17(1):44. [DOI][PubMed][PMC]
9. Yao H, Song M, Zhang H, Li Y, Chen D, Li Y, et al. NSUN2/ALYREF-medicated M5C-modified circRNA505 regulates the proliferation, differentiation, and glycolysis of antler chondrocytes via the miRNA-127/p53 axis and LDHA. Int J Biol Macromol. 2025;309:142527. [DOI]
10. Schmidt D, Wilson MD, Spyrou C, Brown GD, Hadfield J, Odom DT. ChIP-seq: Using high-throughput sequencing to discover protein-DNA interactions. Methods. 2009;48(3):240-248. [DOI]
11. Adams G. A beginner's guide to RT-PCR, qPCR and RT-qPCR. Biochemist. 2020;42(3):48-53. [DOI]
12. Wei MM, Wang L, Zhao BW, Su XR, You ZH, Huang DS. Integrating transformer and graph attention network for circRNA-miRNA interaction prediction. IEEE J Biomed Health Inform. 2025;29(8):6105-6113. [DOI]
13. Liao Q, Liu X, Zhao W, Tong Y, Xu F, Liu X, et al. IRGL-RRI: Interpretable graph representation learning for plant RNA-RNA interaction discovery. Front Plant Sci. 2025;16:1617495. [DOI][PubMed][PMC]
14. Cao C, Li M, Wang C, Xu L, Zou Q, Wang Y, et al. DGCLCMI: A deep graph collaboration learning method to predict circRNA-miRNA interactions. BMC Biol. 2025;23(1):104. [DOI]
15. Li YC, You ZH, Yu CQ, Wang L, Hu L, Hu PW, et al. DeepCMI: A graph-based model for accurate prediction of circRNA-miRNA interactions with multiple information. Brief Funct Genomics. 2024;23(3):276-285. [DOI]
16. Wei M, Wang L, Su X, Zhao B, You Z. Multi-hop graph structural modeling for cancer-related circRNA-miRNA interaction prediction. Pattern Recognit. 2026;170:112078. [DOI]
17. Liu L, Wei Y, Zhang Q, Zhao Q. SSCRB: Predicting circRNA-RBP interaction sites using a sequence and structural feature-based attention model. IEEE J Biomed Health Inform. 2024;28(3):1762-1772. [DOI]
18. Cao C, Wang C, Dai Q, Zou Q, Wang T. CRBPSA: CircRNA-RBP interaction sites identification using sequence structural attention model. BMC Biol. 2024;22(1):260. [DOI][PubMed][PMC]
19. Yao W, Bai J, Liao W, Chen Y, Liu M, Xie Y. From CNN to transformer: A review of medical image segmentation models. J Imaging Inform Med. 2024;37(4):1529-1547. [DOI][PubMed][PMC]
20. Long J, Shelhamer E, Darrell T. Fully convolutional networks for semantic segmentation. In: 2015 IEEE Conference on Computer Vision and Pattern Recognition (CVPR); 2015 Jun 7-12; Boston, USA. Piscataway: IEEE; 2015. p. 3431-3440. [DOI]
21. Wang S, He Y, Chen Z, Zhang Q. FCNGRU: Locating transcription factor binding sites by combing fully convolutional neural network with gated recurrent unit. IEEE J Biomed Health Inform. 2022;26(4):1883-1890. [DOI][PubMed]
22. Zhang Q, He Y, Wang S, Chen Z, Guo Z, Cui Z, et al. Base-resolution prediction of transcription factor binding signals by a deep learning framework. PLoS Comput Biol. 2022;18(3):e1009941. [DOI][PubMed][PMC]
23. Feng J, Chen W, Dong X, Wang J, Mei X, Deng J, et al. CSCD2: An integrated interactional database of cancer-specific circular RNAs. Nucleic Acids Res. 2022;50(D1):D1179-D1183. [DOI][PubMed][PMC]
24. Tang G, Xing H, Yao D, Zhan X, Li X. GGCRB: A graph neural network approach for predicting CircRNA-RBP interactions using structural and sequence features. ACS Omega. 2025;10(30):33662-33674. [DOI][PubMed][PMC]
25. Liu N, Zhang Y. A deep learning approach based on molecular graph features and residual blocks to predict interaction sites between CircRNA and RBP. Biochem Biophys Res Commun. 2025;785:152655. [DOI]
26. Yang Y, Hou Z, Ma Z, Li X, Wong KC. iCircRBP-DHN: Identification of circRNA-RBP interaction sites using deep hierarchical network. Brief Bioinform. 2021;22(4):bbaa274. [DOI]
27. Liao W, He J, Disoma C, Hu Y, Li J, Chen G, et al. Hsa_circ_0107593 suppresses the progression of cervical cancer via sponging hsa-miR-20a-5p/93-5p/106b-5p. Front Oncol. 2020;10:590627. [DOI][PubMed][PMC]
28. Jiang X, Chen D. Circular RNA hsa_circ_0000658 inhibits osteosarcoma cell proliferation and migration via the miR-1227/IRF2 axis. J Cell Mol Med. 2021;25(1):510-520. [DOI][PubMed][PMC]
29. Zhang Y, Liu S, Wu C, Gao X, Zhao H, Li O, et al. Exosomal circ_0001583 drives glioblastoma cell advancement through the miR-647/CKAP2L pathway. Mol Neurobiol. 2025;62(8):10687-10706. [DOI]
30. Chen B, Feng H, Zou CG, Tang H. Effects of circTRIM33-12 on proliferation, apoptosis and epithelial-mesenchymal transition of brain glioma cells by regulating miR-191/DAB2 axis. J Reg Anat Oper Surg. 2024;33(1):36-43,8. Chinese. [DOI]
31. Ye W, Chen L, Feng C, Liang T. CircMYLK promotes the growth, migration, invasion, and survival of bladder cancer cells by upregulating CCND3 level via competitively binding to miR-34a. Drug Dev Res. 2021;82(8):1206-1216. [DOI][PubMed]
32. Shen D, Zhao H, Zeng P, Ge M, Shrestha S, Zhao W. Circular RNA circ_0001459 accelerates hepatocellular carcinoma progression via the miR-6165/IGF1R axis. Ann N Y Acad Sci. 2022;1512(1):46-60. [DOI][PubMed][PMC]

33. Cui S, Qian Z, Chen Y, Li L, Li P, Ding H. Screening of up- and downregulation of circRNAs in HBV-related hepatocellular carcinoma by microarray. Oncol Lett. 2018;15(1):423-432. [DOI][PubMed][PMC]
34. Lin M, Zheng Y, Li Q, Liu Y, Xu Q, Li Y, et al. Circular RNA expression profiles significantly altered in UVA-irradiated human dermal fibroblasts. Exp Ther Med. 2020;20(6):163. [DOI][PubMed][PMC]
35. Hei R, Chen J, Zhang X, Bian H, Chen C, Wu X, et al. CircNRIP1 acts as a sponge of miR-1200 to suppress osteosarcoma progression via upregulation of MIA2. Am J Cancer Res. 2022;12(6):2833-2849. [PubMed][PMC]
36. Aslani S, Kalantary-Charvadeh A, Morovat P, Abbasalipourkabir R, Nourmohammadi I, Emami Razavi A, et al. Integrated bioinformatics and tissue-based validation reveal the oncogenic role of hsa_circ_0043256 and hsa_circ_0004789 in gastric cancer. Biochem Biophys Rep. 2026;45:102442. [DOI][PubMed][PMC]
37. Li Y, Ren S, Xia J, Wei Y, Xi Y. EIF4A3-induced circ-BNIP3 aggravated hypoxia-induced injury of H9c2 cells by targeting miR-27a-3p/BNIP3. Mol Ther Nucleic Acids. 2020;19:533-545. [DOI][PubMed][PMC]
38. Bi J, Pu Y, Yu X. Exosomal circ_0004136 enhances the progression of pediatric acute myeloid leukemia depending on the regulation of miR-570-3p/TSPAN3 axis. Anticancer Drugs. 2021;32(8):802-811. [DOI][PubMed]
39. Zhu M, Lian C, Chen G, Zou P, Qin BG. CircRNA FUT10 regulates the regenerative potential of aged skeletal muscle stem cells by targeting HOXA9. Aging. 2021;13(13):17428-17441. [DOI][PubMed][PMC]
40. Kong X, Xu R, Wang W, Zeng M, Li Y, Lin M, et al. CircularLRRC7 is a potential tumor suppressor associated with miR-1281 and PDXP expression in glioblastoma. Front Mol Biosci. 2021;8:743417. [DOI][PubMed][PMC]
41. Jia C, Yao Z, Lin Z, Zhao L, Cai X, Chen S, et al. circNFATC3 sponges miR-548I acts as a ceRNA to protect NFATC3 itself and suppressed hepatocellular carcinoma progression. J Cell Physiol. 2021;236(2):1252-1269. [DOI]
42. Sun S, Li C, Cui K, Liu B, Zhou M, Cao Y, et al. Hsa_circ_0062682 promotes serine metabolism and tumor growth in colorectal cancer by regulating the miR-940/PHGDH axis. Front Cell Dev Biol. 2021;9:770006. [DOI][PubMed][PMC]
43. Chen W, Ji Y. CircC6orf132 facilitates proliferation, migration, invasion, and glycolysis of gastric cancer cells under hypoxia by acting on the miR-873-5p/PRKAA1 axis. Front Genet. 2021;12:636392. [DOI]
44. Jia G, Lv D, Ni S. Circ_0061140 potentiates clear cell renal cell carcinoma progression via the microRNA-126-5p/ADAM9 axis. Mol Biotechnol. 2024;66(12):3688-3699. [DOI]
45. Meng L, Chang S, Sang Y, Ding P, Wang L, Nan X, et al. Circular RNA circCCDC85A inhibits breast cancer progression via acting as a miR-550a-5p sponge to enhance MOB1A expression. Breast Cancer Res. 2022;24(1):1. [DOI][PubMed][PMC]
46. Wang LL, Zong ZH, Liu Y, Guan X, Chen S, Zhao Y. CircRhoC promotes tumorigenicity and progression in ovarian cancer by functioning as a miR-302e sponge to positively regulate VEGFA. J Cell Mol Med. 2019;23(12):8472-8481. [DOI][PubMed][PMC]
47. Sun J, Wu H, Luo J, Qiu Y, Li Y, Xu Y, et al. CircTBC1D22A inhibits the progression of colorectal cancer through autophagy regulated via miR-1825/ATG14 axis. iScience. 2024;27(3):109168. [DOI][PubMed][PMC]
48. Zhang C, Gao C, Di X, Cui S, Liang W, Sun W, et al. Hsa_circ_0123190 acts as a competitive endogenous RNA to regulate APLNR expression by sponging hsa-miR-483-3p in lupus nephritis. Arthritis Res Ther. 2021;23(1):24. [DOI][PubMed][PMC]
49. Zhu M, Wang Y, Wang F, Li L, Qiu X. CircFBXL5 promotes the 5-FU resistance of breast cancer via modulating miR-216b/HMGA2 axis. Cancer Cell Int. 2021;21(1):384. [DOI][PubMed][PMC]
50. Zhu X, Li W, Lu M, Shang J, Zhou J, Lin L, et al. M^6A demethylase FTO-stabilized exosomal circBRCA1 alleviates oxidative stress-induced granulosa cell damage via the miR-642a-5p/FOXO1 axis. J Nanobiotechnology. 2024;22(1):367. [DOI][PubMed][PMC]
51. Liu T, Ye P, Ye Y, Lu S, Han B. Circular RNA hsa_circRNA_002178 silencing retards breast cancer progression via microRNA-328-3p-mediated inhibition of COL1A1. J Cell Mol Med. 2020;24(3):2189-2201. [DOI][PubMed][PMC]
52. Wang C, Zhou M, Zhu P, Ju C, Sheng J, Du D, et al. IGF2BP2-induced circRUNX1 facilitates the growth and metastasis of esophageal squamous cell carcinoma through miR-449b-5p/FOXP3 axis. J Exp Clin Cancer Res. 2022;41(1):347. [DOI][PubMed][PMC]
53. Zhou R, Miao S, Xu J, Sun L, Chen Y. Circular RNA circ_0000020 promotes osteogenic differentiation to reduce osteoporosis via sponging microRNA miR-142-5p to up-regulate Bone Morphogenetic Protein BMP2. Bioengineered. 2021;12(1):3824-3836. [DOI][PubMed][PMC]
54. Li Q, Tian Y, Liang Y, Li C. CircHIPK3/miR-876-5p/PIK3R1 axis regulates regulation proliferation, migration, invasion, and glutaminolysis in gastric cancer cells. Cancer Cell Int. 2020;20:391. [DOI][PubMed][PMC]
55. Zhu CL, Sha X, Wang Y, Li J, Zhang MY, Guo ZY, et al. Circular RNA hsa_circ_0007142 is upregulated and targets miR-103a-2-5p in colorectal cancer. J Oncol. 2019;2019:9836819. [DOI]
56. Du W, Li Y, Wang X, Xie S, Ci H, Zhou J, et al. Circular RNA circESYT2 serves as a microRNA-665 sponge to promote the progression of hepatocellular carcinoma through ENO2. Cancer Sci. 2024;115(8):2659-2672. [DOI][PubMed][PMC]

Publisher's Note

Science Exploration remains a neutral stance on jurisdictional claims in published maps and institutional affiliations. The views expressed in this article are solely those of the author(s) and do not reflect the opinions of the Editors or the publisher.